ACS OMEGA

Open Access

This article is licensed under CC-BY 4.0

http://pubs.acs.org/journal/acsodf

Article

Mechanism of Solid Ammonia Stabilization at Ambient Temperature: Insights from Thermodynamics, Phonon Calculation, and Micromechanics

Masao Morishita,* Terumasa Tadano, Yusuke Matsuoka, and Taichi Abe

Cite This: *ACS Omega* 2025, 10, 57684−57691

Read Online

ACCESS | Metrics & More | Article Recommendations | Supporting Information

ABSTRACT: The stabilization of low-temperature solid-state ammonia at ambient temperature was recently achieved by confining fine crystals within a boric acid glass matrix through freeze-drying using liquid nitrogen, opening a new frontier for hydrogen storage materials. We determined the stabilization mechanism using a thermodynamic model supported by first-principles phonon calculation and pressure analysis based on micromechanics. Phonon calculation revealed vibrational densities of states (DOS) for the intermolecular translational and rotational modes of NH_3 molecules, as well as intramolecular librational and bending modes of hydrogen atoms. Simulations incorporating the computed DOS into a thermodynamic model reveal that sub-GPa pressure is exerted on ammonia crystals by the surrounding glass matrix. Micromechanical analysis confirms that this hydrostatic stress originates from the difference in thermal expansion coefficients. The results suggest that ammonia crystals are stabilized by this pressure. Thus, our findings provide a new strategy for stabilizing nonequilibrium phases at ambient temperature, opening new frontiers for hydrogen storage materials.

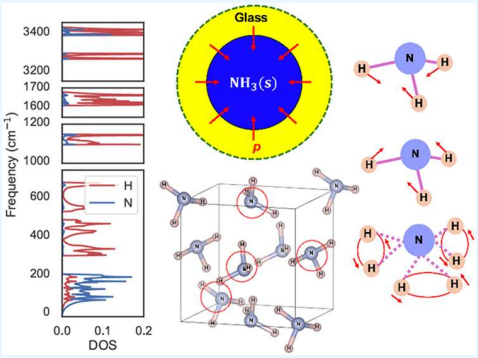

1. INTRODUCTION

Alternative energy resources such as solar photovoltaic technology and wind power are widely explored to reduce CO_2 emissions from fossil fuels. However, the consistent supply of these resources is limited because of their reliance on weather and geography limits consistent supply. This has increased the difficulty of meeting growing energy demands and intensified the need for alternative energy storage solutions. One promising alternative is green hydrogen, which is produced by water electrolysis using renewable energy. This hydrogen can be reconverted into electricity using fuel cells or used directly as a combustion fuel. However, the energy density of $H_2(g)$ is nearly 1/3000th that of gasoline due to its low volumetric density.[1] Moreover, storing and transporting $H_2(l)$ is challenging because of its extremely low boiling point ($T^{\circ}_{b.p.}$ = 20 K) and the high cost of liquefaction needed to increase its energy density.

Ammonia is a promising hydrogen carrier,[2−11] and when produced from green hydrogen, it is termed green ammonia. At ambient temperature, it can be stored as a liquid in standard cylinders due to its liquefaction at ∼8 atm and 20 °C.[12] Ammonia is industrially produced via the Haber−Bosch process,[2] which uses an iron catalyst under high temperature and pressure to combine hydrogen and nitrogen. Additionally, ammonia production has been explored via the cleavage of the strong N−N bonds in $N_2(g)$ using electrolysis,[3−5] discharge,[6] and surface plasmon resonance.[7] Conversely, ammonia can be converted into $H_2(g)$ and $N_2(g)$ using catalysts such as Ni,[8,9] Ru,[9] and CaNH,[10] while the generated $H_2(g)$ is separated using membranes.[11] However, the storage and transport of ammonia remain challenging as it is a deleterious substance. Damage to pressurized vessels during transit releases toxic ammonia gas, posing serious risks and even fatalities. In our previous study,[13] while exploring a new synthesis route for ammonia borane (NH_3BH_3),[14−17] we serendipitously discovered that low-temperature solid-state ammonia can be stabilized at ambient temperature. Specifically, we successfully synthesized $NH_3(s)$, preserved within a glass matrix, facilitated by freeze-drying an ice of boric acid and ammonium aqueous solution using liquid nitrogen at 77 K. The resulting $NH_3(s)$, with a lattice constant of 0.5165 nm,[13] remained stable at ambient temperature and pressure, confirmed using X-ray diffraction (XRD), Raman spectroscopy, chemical analyses, gas and ion chromatography, and approximate thermodynamic modeling.[13] This $NH_3(s)$ is a potentially safe hydrogen storage material due to its odorless nature.[13]

Received: September 4, 2025
Revised: October 23, 2025
Accepted: October 30, 2025
Published: November 17, 2025

Downloaded via NATL INST FOR MATLS SCIENCE (NIMS) on December 3, 2025 at 01:07:49 (UTC).
See https://pubs.acs.org/sharingguidelines for options on how to legitimately share published articles.

ACS Publications

© 2025 The Authors. Published by American Chemical Society

https://doi.org/10.1021/acsomega.5c09165
ACS Omega 2025, 10, 57684−57691

Investigations on ammonia stabilization contribute to the progress of planetary exploration,[18,19] life sciences,[20] and energy science.[2−11] To understand the wide-ranging thermodynamic conditions in these areas, phase diagrams mapping equilibrium states as a function of temperature (T), pressure (p), and related properties have been investigated.[12,19,21−32] In this study, the stabilization mechanism of NH_3(s) confined in a glass matrix was investigated under ambient conditions to ensure its safety, associating it with the related phase equilibria properties.[12,19,21−32] Specifically, the phonon densities of states (DOS) were theoretically calculated for solid-state ammonia in its ground state. Using the Debye−Einstein function based on these DOS, the standard Gibbs energy of formation ($\Delta_f G^\circ_m$) at 298.15 K was calculated to clarify why NH_3(s) remains stable at ambient temperature. The $\Delta_f G^\circ_m$ data indicates that the glass matrix exerts sub-GPa-order pressure on NH_3(s), stabilizing it in a quasi-equilibrium state. Micromechanical simulations confirmed the presence of such pressures, consistent with the thermodynamic model predictions.

2. METHODS

2.1. Formation Mechanism of NH_3(s). Figure 1 shows the process for confining NH_3(s) within the boric acid glass

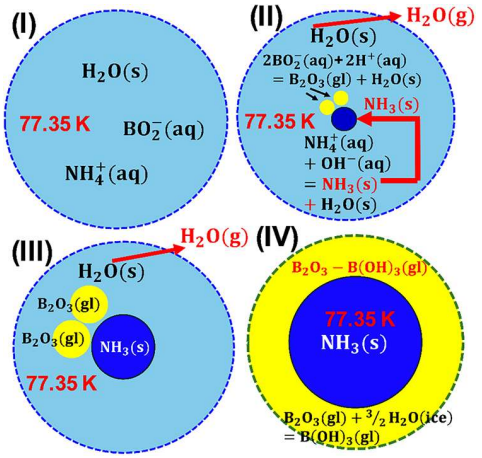

Figure 1. Schematic of the formation mechanism of confined NH_3(s) at 77 K.

matrix, termed B_2O_3(gl)−$B(OH)_3$(gl), using a freeze-drying technique:[13] (I) An aqueous solution of ammonium boric acid, prepared from commercial NH_3(aq) and B_2O_3(s) at ambient temperature, is frozen at 77 K using liquid nitrogen as a refrigerant. Ammonium ions (NH_4^+(aq)) and metaboric acid anions (BO_2^-) are distributed within the ice matrix of H_2O(s). (II) Upon vacuum evacuation, H_2O(s) sublimates preferentially to satisfy charge neutrality, whereas NH_4^+(aq) condenses, failing to meet charge balance. After sufficient condensation, NH_3(s) nucleates as the equilibrium phase at 77 K via proton transfer (H^+(aq)) from NH_4^+(aq) to OH^-(aq), forming H_2O(s). Similarly, BO_2^-(aq) condenses. Subsequently, B_2O_3(gl) nucleates via O^{2-}(aq) transfer from BO_2^-(aq) to neighboring H^+(aq), also forming H_2O(s). (III) NH_3(s) and B_2O_3(gl) particles proceed to grow. (IV) A certain amount of B_2O_3(gl) hydrates to form $B(OH)_3$(gl), while the remaining H_2O(s) sublimates. As a result, NH_3(s) is confined in the boric acid glass matrix, B_2O_3(gl)−$B(OH)_3$(gl). Once within this characteristic structure, NH_3(s) remains stable upon heating to ambient temperature. Chemical analysis revealed the sample contains 37 mol % NH_3(s), 5 mol % $NH_4B_5O_8{\cdot}4H_2O$(s), 10 mol % B_2O_3(gl), and 48 mol % $B(OH)_3$(gl). The average diameter of NH_3(s) is 37.8 nm, as determined by applying the full width at half-maximum (fwhm) of the main XRD peak[13] to the Scherrer's equation.[33] Based on the lattice constant of NH_3(s) confined in the glass matrix (0.5165 nm),[13] its density is 30 percent higher than that of liquid ammonia in pressurized vessels.

2.2. Thermodynamic Evaluation, Phonon Calculation, and Micromechanical Analysis. To determine the phase stability of NH_3(s) at ambient temperature, its $\Delta_f G^\circ_m$ value at 298.15 K needs to be calculated. We estimated it based on a thermodynamic cycle incorporating existing thermodynamic data as

$$\begin{aligned}&\Delta_f G^\circ_m(NH_3(s), 298.15K)\\ &= \Delta_f G^\circ_m(NH_3(s), 195.4K) + \int_{195.4}^{298.15} C^\circ_{p,m}(NH_3(s))dT\\ &- \frac{1}{2}\int_{195.4}^{298.15} C^\circ_{p,m}(N_2(g))dT - \frac{3}{2}\int_{195.4}^{298.15} C^\circ_{p,m}(H_2(g))dT\\ &- T\left\{\int_{195.4}^{298.15}\frac{C^\circ_{p,m}(NH_3(s))}{T}dT - \frac{1}{2}\int_{195.4}^{298.15}\frac{C^\circ_{p,m}(N_2(g))}{T}dT\right.\\ &\left.- \frac{3}{2}\int_{195.4}^{298.15}\frac{C^\circ_{p,m}(H_2(g))}{T}dT\right\}\end{aligned} \quad (1)$$

where the heat capacities of gaseous nitrogen and hydrogen, $C^\circ_{p,m}(N_2(g))$ and $C^\circ_{p,m}(H_2(g))$, respectively, were obtained from CODATA.[34]

At the melting point (195.4 K), the value of $\Delta_f G^\circ_m(NH_3(s), 195.4\ K)$ was determined by using $C^\circ_{p,m}(N_2(g))$ and $C^\circ_{p,m}(H_2(g))$, along with the heat capacities of gaseous[34] and liquid ammonia,[35] $C^\circ_{p,m}(NH_3(g))$ and $C^\circ_{p,m}(NH_3(l))$, as well as the standard Gibbs energy of formation of gaseous ammonia at 298.15 K, $\Delta_f G^\circ_m(NH_3(g), 298.15\ K)$,[34] based on the thermodynamic cycle expressed by eqs (S1)−(S4) (see the Supporting Information (SI) for all lettered equations). Consequently, to determine $\Delta_f G^\circ_m(NH_3(s), 298.15\ K)$, the heat capacities of solid ammonia, $C^\circ_{p,m}(NH_3(s))$, above the melting point (195.4−300 K) should be estimated.

Overstreet and Giauque[35] previously measured $C^\circ_{p,m}(NH_3(s))$ at 15−190 K using adiabatic calorimetry. We fitted their data in the 60−190 K range using the Debye−Einstein function[36−44] expressed as eq 2.

$$\begin{aligned}C^\circ_{p,m} &= 3\alpha R\left\{lD\left(\frac{\Theta_D}{T}\right) + mE_1\left(\frac{\Theta_{E_1}}{T}\right) + nE_2\left(\frac{\Theta_{E_2}}{T}\right)\right\} + A_1T\\ &+ A_2T^3,\ 71.58\ K < T < 300\ K\end{aligned} \quad (2)$$

The fitted function was used to estimate the $C^\circ_{p,m}(NH_3(s))$ at 195.4−300 K, and $\Delta_f G^\circ_m(NH_3(s), 298.15\ K)$ was calculated. Here, $D\left(\frac{\Theta_D}{T}\right)$ is the Debye function accounting for the intermolecular translational and rotational modes of ammonia molecules in the solid crystal, NH_3(m), whereas $E_1\left(\frac{\Theta_{E_1}}{T}\right)$ and $E_2\left(\frac{\Theta_{E_2}}{T}\right)$ are Einstein functions[45] representing the intramolecular librational and bending modes of hydrogen atoms, H(a). The characteristic temperatures, Θ_D, Θ_{E_1}, and Θ_{E_2}, correspond to these inter- and intramolecular vibrational

https://doi.org/10.1021/acsomega.5c09165
ACS Omega 2025, 10, 57684−57691

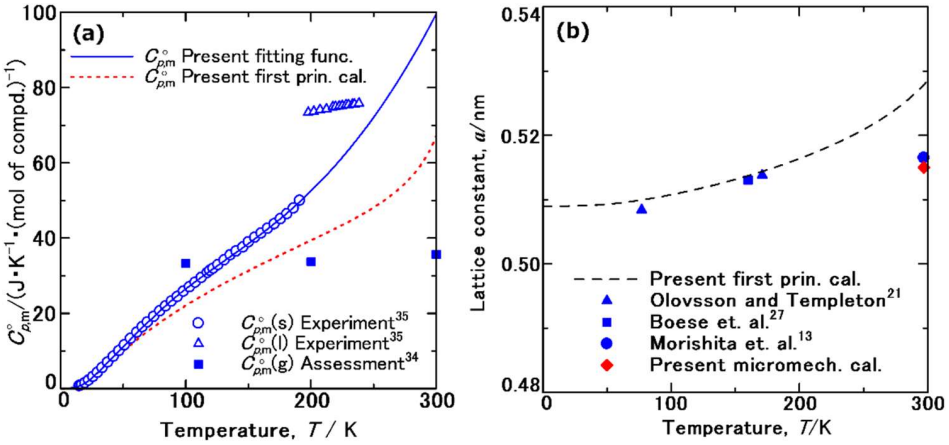

Figure 2. (a) $C^\circ_{p,m}$ data for ammonia: solid (open circles) and liquid (open triangles) measured by Overstreet and Giauque (Adapted in J. Am. Chem. Soc., **1937**, 59, 254−259);[35] gas phase (solid squares) from CODATA;[34] solid (solid line) from the Debye−Einstein function (eqs 2−4 and Table S2); solid (dotted line) simulated from our first-principles calculations. (b) Lattice constants for solid ammonia: from low-temperature in situ XRD of pristine samples by Olovson and Templeton[21] (solid triangle) and Boese et al.[27] (solid square); from XRD at 297.15 K using NH_3(s) confined in a glass matrix from our previous work[13] (solid circle); from our first-principles phonon calculation (dotted line) and micromechanical simulation (solid diamond).

modes. The sum of the T-linear term (A_1T) and T-cubed term (A_2T^3) was used as an adjusting parameter, while the T-squared term (A_2T^2) in the sum is generally adopted to adjust thermal expansion.[36−44] However, calculating $C^\circ_{p,m}(NH_3(s))$ is complicated due to extra contributions from the orientational disorder of molecules[46−48] and precursory phenomenon of melting.[49] The T-cubed term (A_2T^3) was found to be phenomenologically preferable for including thermal expansion,[36−44] the orientational disorder of molecules,[46−48] and precursory phenomenon of melting[49] described later. α represents the number of atoms per NH_3(m) (i.e., 4).

The coefficients l, m, and n in eq 2, representing the relative contributions of intermolecular translational and rotational modes and intramolecular librational and bending modes, were determined from first-principles phonon calculations, which were conducted using the ALAMODE[50] code in combination with the Vienna Ab initio Simulation Package (VASP)[51,52] using eqs (S5)−(S8) (see the SI for computational details). For the exchange-correlation functional, the generalized gradient approximation of Perdew−Burke−Ernzerhof (GGA-PBE)[53] was employed with the DFT-D4 dispersion correction.[54]

To complete the thermodynamic profile for NH_3(s), low-temperature $C^\circ_{p,m}(NH_3(s))$ data reported by Overstreet and Giauque[35] were fitted to polynomial functions (eqs 3 and 4). To minimize fitting error, the temperature ranges were divided into three segments.[36−44]

$$C^\circ_{p,m} = \gamma T + \sum_{j=3,5,7,9,11} B_i T^i, \quad 0\ \mathrm{K} < T < 33.18\ \mathrm{K} \tag{3}$$

$$C^\circ_{p,m} = \sum_{j=0}^{6} C_j T^j, \quad 33.18\ \mathrm{K} < T < 71.58\ \mathrm{K} \tag{4}$$

γ and B_i in eq 3 are coefficients representing electronic[45,55] and vibrational[45] contributions to $C^\circ_{p,m}$ at very low temperatures, respectively, while C_j in eq 4 is an empirical coefficient for a power-law temperature function expressing $C^\circ_{p,m}$ in the intermediate temperature range. The intersection points between eqs 3 and 4, i.e., 33.18 K, and eqs 2 and 4, i.e., 71.58 K, were determined using the Newton−Raphson method.[37−43]

The likely cause of NH_3(s) stabilization at ambient temperature is the pressure exerted by the glass matrix, resulting from a thermal expansion difference. Therefore, pressure effects were also investigated. As a fundamental thermodynamic model, the pressure required for the phase transition from gas to solid via liquid was evaluated thermodynamically. At 298.15 K, the condensation pressure was calculated using eqs (S9)−(S14) (see the SI), assuming that pressurization has a negligible effect on the chemical potential of the condensed phase.[56] The freezing pressure was subsequently determined using eqs (S15)−(S18) (see the SI). Consequently, the total pressure required for gas-to-solid transition via the liquid state was defined as the sum (eq (S19)) of the values expressed as eqs (S14) and (S18) (see the SI).

A micromechanical simulation was conducted to confirm that the pressure predicted by this thermodynamic simulation was indeed exerted by the glass matrix on NH_3(s). To evaluate the thermal stress acting on the solid NH_3 particles confined within the boric glass matrix, changes in the lattice constant of NH_3 and stress induced in the boric glass matrix surrounding the NH_3 particles, we performed simulations based on the phase-field micromechanical elasticity theory.[57,58] The calculations consider the constrained thermal expansion of spherical NH_3(s) particles within the glass matrix. Here, we adopted the physical properties of pristine B_2O_3 since those of the glass matrix composed of 37 mol % NH_3(s), 5 mol % $NH_4B_5O_8\cdot 4H_2O$(s), 10 mol % B_2O_3(gl), and 48 mol % $B(OH)_3$(gl) are unknown. The elastic modulus of pristine B_2O_3 was adopted from the experimental data of Ramos et al.[59] For the purpose of simplification, we neglected its low thermal expansion coefficient, approximately 15 × 10^{-6} K^{-1} in the 100−300 K range.[60] Incidentally, negative thermal expansion has been reported for B_2O_3 at lower temperatures.[61] For solid NH_3(s), the thermal expansion coefficient and elastic constant were estimated from the present first-principles calculation. The hydrostatic stress, σ_{hydro}, was simulated considering theories for

https://doi.org/10.1021/acsomega.5c09165
ACS Omega 2025, 10, 57684−57691

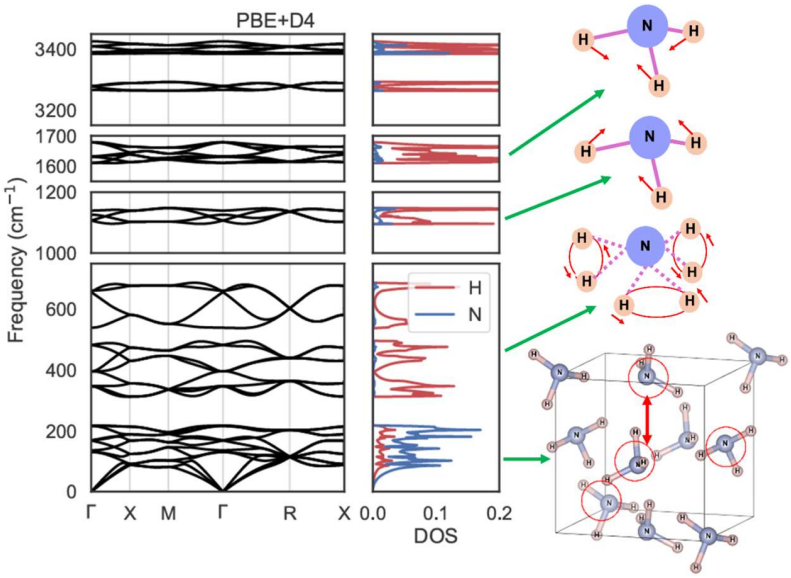

Figure 3. Calculated phonon dispersion and densities of states (DOS) for type I NH_3(s). Schematic figures of vibrational modes representing each energy region are also illustrated.

geometric morphologies.[62] This analysis is further discussed in the SI, expressed as eqs (S20)−(S27) and Table S1.

3. RESULTS AND DISCUSSION

Figure 2a shows the $C^{\circ}_{p,m}$ data for the solid (open circles) and liquid phases (open triangles) of ammonia, as measured by Overstreet and Giauque using adiabatic calorimetry.[35] The melting of NH_3(s) into NH_3(l) was observed at 195.4 K, and a discontinuous increase in $C^{\circ}_{p,m}$ during this first-order transition was found. Moreover, the transition from NH_3(l) to NH_3(g) was observed at 239.7 K.[35] The $C^{\circ}_{p,m}$ data for gaseous ammonia (solid squares) were evaluated from 4000 to 100 K based on statistical thermodynamic estimates from CODATA.[34]

The solid line in Figure 2a represents the values calculated from the fitting functions defined by eqs 2−4. Their coefficients are summarized in Table S2 (see the SI for all lettered tables). The calculated data are consistent with experimental values,[35] and the differences between them ($u_{fit}(C^{\circ}_{p,m})$) were found to be within one percent and are shown in Figure S1 (see the SI).

The $C^{\circ}_{p,m}$ data for NH_3(s) above its melting point of 195.4 K were estimated by extrapolating the Debye−Einstein function (eq 2). The slope of the extrapolated $C^{\circ}_{p,m}$ curve as a function of temperature increased above 195.4 K. The optimized Debye−Einstein function appeared to reflect the change in intermolecular interactions among NH_3(m) molecules at the melting point.

Figure 2b shows the lattice constant of pristine NH_3(s) as a function of temperature, determined from first-principles phonon calculations based on PBE + D4[54] To investigate the effect of the exchange-correlation functional on the predicted lattice constants, we also conducted the calculations using PBEsol+D4,[54] PBEsol,[63] r^{2}SCAN,[64] and r^{2}SCAN +rVV10.[65] As shown in Figure S2 in the SI, the calculated values using PBE+D4[54] were in closest agreement with experimental data.[21,27] A similar increase in the slope of the lattice constant as a function of temperature was observed above the melting point (195.4 K). The mechanism of this increase appears to be similar to that of the $C^{\circ}_{p,m}$ data (Figure 2a), reflecting the changes in intermolecular interactions among NH_3(m) molecules.

Figure 3 shows the phonon dispersion and DOS corresponding to the vibrational modes of NH_3(s) using PBE+D4.[54] By analyzing the computed phonon polarization vectors, the characteristic vibrational modes in each energy region were identified as follows: (I) Modes at 0−217 cm^{-1} are the intermolecular translation and rotation of NH_3(m); (II) Modes at 313−687 cm^{-1} are the intramolecular librational vibration of H(a); (III-A) Modes at 1096−1147 cm^{-1} are the symmetric bending vibration of H(a); (III−B) Modes at 1611−1678 cm^{-1} are the antisymmetric bending vibration of H(a); (IV-A) Modes at 3264−3292 cm^{-1} are the antisymmetric stretching vibration of H(a); (IV−B) Modes at 3385−3425 cm^{-1} are the symmetric stretching vibration of H(a).

To construct the Debye−Einstein function (eq 2) for extrapolating the $C^{\circ}_{p,m}$ data from Overstreet and Giauque,[35] the relative ratios l, m, and n were determined based on the vibrational modes described above: (a) Because $D\left(\frac{\Theta_D}{T}\right)$ is defined as the acoustic mode due to coupled atomic motion,[45] it is appropriate to evaluate the intermolecular translational and rotational modes of NH_3(m) at a lower wavenumber range (0−217 cm^{-1}). The relative ratio of the sum of the partial densities of states (PDOS) of N(a) and H(a) at 0−217 cm^{-1} to the full DOS contributing to the $C^{\circ}_{p,m}$ was 0.33270. Thus, l, representing the relative ratio of $D\left(\frac{\Theta_D}{T}\right)$, was assigned the value of 0.33270. (b) Optical modes in the 313−687 cm^{-1} range, associated with the librational vibration of H(a), were evaluated using $E_1\left(\frac{\Theta_{E_1}}{T}\right)$. The relative PDOS ratio was 0.33378, which was used for m, representing the relative ratio of $E_1\left(\frac{\Theta_{E_1}}{T}\right)$. (c) $E_2\left(\frac{\Theta_{E_2}}{T}\right)$ was used to evaluate the sum of the optical modes at 1096−1147 and 1611−1678 cm^{-1}, corresponding to the symmetric and antisymmetric vibrations of H(a). The relative PDOS ratio was 0.33349, and this was adopted for n, representing the relative ratio of $E_2\left(\frac{\Theta_{E_2}}{T}\right)$. The

https://doi.org/10.1021/acsomega.5c09165
ACS Omega 2025, 10, 57684−57691

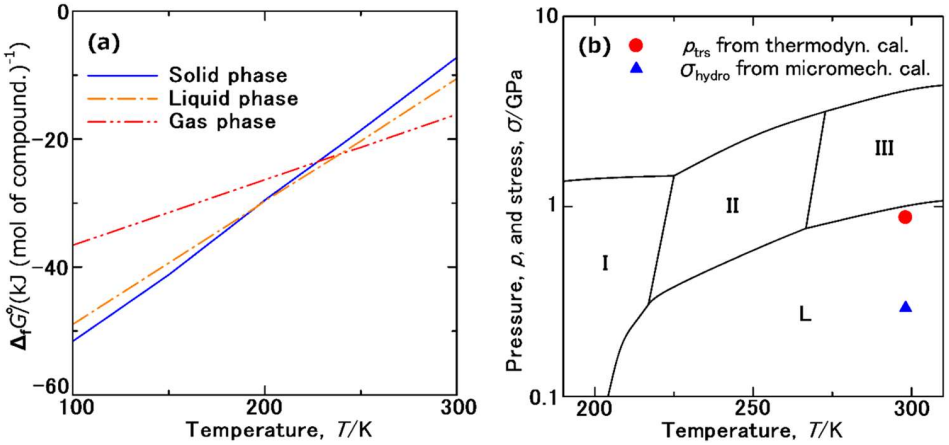

Figure 4. (a) $\Delta_f G^\circ_m$ data at 100−300 K for solid (solid line), liquid (dashed-dotted line), and gaseous ammonia (dashed double-dotted line). (b) Pressure, p_{trs}, and hydrostatic stress, σ_{hydro}, required for the phase transition based on our thermodynamic calculations (solid circle) and micromechanical simulation (solid triangle) on the $p-T$ phase diagram of ammonia.[26] (Adapted in part in Phys. Rev. Lett., **1995**, 76, 74−77).

wavenumber ranges 3264−3292 and 3385−3425 cm^{-1}, corresponding to antisymmetric and symmetric stretching vibrations, exceed the detection limits of $C^\circ_{p,m}$ measurements; therefore, these were excluded from the model. As a result, the Debye−Einstein function incorporating these *l*, *m*, and *n* values showed good agreement with the experimental data of Overstreet and Giauque.[35]

The $C^\circ_{p,m}$ data determined from first-principles calculations are depicted with a dotted line in Figure 2a and solid lines in Figure S3. Popov et al.[48] measured the $C^\circ_{p,m}$ data for NH_3(s) and confirmed the accuracy of the data of Overstreet and Giauque[35] noting that extra heat capacity was generated due to the orientational disorder of NH_3(s) molecules. Additional contributions to the heat capacity are also known to occur due to the precursory phenomena of melting.[49] The theoretical values were found to be smaller than the experimental data.[35] We confirmed that the calculated $C^\circ_{p,m}$ values are consistently smaller than the experimental ones for all the considered exchange-correlation functionals. Hence, the underestimation is potentially due to contributions not only from the orientational disorder of NH_3 molecules[46−48] or anharmonic effects but also from the precursory phenomenon of melting,[49] which is not captured in the present phonon calculations.

Figure 4a shows the $\Delta_f G^\circ_m$ data at 100−300 K for solid, liquid, and gaseous ammonia. Above the boiling point, the $\Delta_f G^\circ_m$ values were more negative in the order of gas, liquid, and solid, consistent with the hierarchy of their phase stability. However, the $\Delta_f G^\circ_m$ data at ambient temperatures for solid ammonia were found to be negative, indicating that it can exist in a quasi-equilibrium state. Thermodynamic data for solid, liquid, and gas phases were summarized in Tables S3 and S4 (see the SI). At 298.15 K, the $\Delta_f G^\circ_m$ data for solid, liquid, and gaseous ammonia were calculated as

$$\Delta_f G^\circ_m(NH_3(s),\ 298.15\ K)/(kJ(mol\ of\ compd.\ )^{-1}) = -7.650 \quad (5)$$

$$\Delta_f G^\circ_m(NH_3(l),\ 298.15\ K)/(kJ(mol\ of\ compd.\ )^{-1}) = -11.104 \quad (6)$$

$$\Delta_f G^\circ_m(NH_3(g),\ 298.15\ K)/(kJ(mol\ of\ compd.\ )^{-1}) = -16.319 \quad (7)$$

From these $\Delta_f G^\circ_m$ values, the Gibbs energies of condensation, $\Delta_{con} G^\circ_m$, freezing, $\Delta_{freez} G^\circ_m$, and phase transition from the gas to solid phase via the liquid phase, $\Delta_{trs} G^\circ_m$, at 298.15 K were estimated as

$$\Delta_{con} G^\circ_m(NH_3,\ 298.15\ K)/(kJ(mol\ of\ compd.\ )^{-1}) = 5.414 \quad (8)$$

$$\Delta_{freez} G^\circ_m(NH_3,\ 298.15\ K)/(kJ(mol\ of\ compd.\ )^{-1}) = 3.255 \quad (9)$$

$$\Delta_{trs} G^\circ_m(NH_3,\ 298.15\ K)/(kJ(mol\ of\ compd.\ )^{-1}) = 8.669 \quad (10)$$

As given by eqs (S14), (S18), and (S19) in the SI, the pressures required for condensation, p_{con}, freezing, p_{con}, and phase transition from the gas to solid phase via the liquid phase, p_{trs}, were estimated as

$$p_{con}(NH_3,\ 298.15\ K)/GPa = 8.88 \times 10^{-4} \quad (11)$$

$$p_{freez}(NH_3,\ 298.15\ K)/GPa = 0.874 \quad (12)$$

$$p_{trs}(NH_3,\ 298.15\ K)/GPa = 0.875 \quad (13)$$

Figure 4b shows the phase diagram of ammonia under high pressure.[26] Complex polymorphs from phase I to phase III were observed in the solid state. Phase I was found to be a cubic crystal ($P2_13$),[21,25−27] corresponding to the NH_3(s) confined in the glass matrix in our previous study.[13] Phase II was identified as a hexagonal crystal ($P6_3/mmc$),[25] while phase III was cubic ($Fm3m$),[23,25,26] representing a structure where the reciprocal rotation of NH_3(m) in phase I decreases the degree of order. When we plotted the p_{trs} value determined from the gas to solid transition via the liquid phase (solid circle in Figure 4b), it was well correlated with the phase boundary between the liquid phase and solid phase III. However, as mentioned above, the NH_3(s) from our previous study[13] was determined to be cubic phase I ($P2_13$),[21,25−27] and not cubic phase III ($Fm3m$).[23,25,26] Various polymorphs of fine particles are generally known to be formed under ambient conditions. Structures of α- and γ- type polymorphs in alumina (Al_2O_3)[66] and rutile- and anatase-type polymorphs in titania (TiO_2)[67] are formed depending on particle size, surface energy and the surface adsorption of moisture. Based on these polymorphs,

https://doi.org/10.1021/acsomega.5c09165
ACS Omega 2025, 10, 57684−57691

the nanocrystal of ammonia cubic phase I[13] is likely to be stable within the glass matrix. Robust B−N bonds are likely to form along the interface between the cubic phase I and the glass matrix. The interfacial energy originating from a B−N bonds is likely to contribute to the configuration of the cubic phase I.

To clarify that p_{trs} acts on solid NH_3 particles, we performed a simulation based on the phase-field micromechanical elasticity theory.[57,58] While lattice parameters obtained from PBE+D4 calculations accurately reproduced previously reported values at low temperatures,[21,27] discrepancies were observed when compared to the lattice constant of solid ammonia in the glass matrix measured at 297 K.[13] This is likely due to the thermal expansion of solid NH_3 particles being elastically constrained by the glass matrix. Hence, the lattice parameter of solid NH_3 particles within the glass matrix, hydrostatic stress, σ_{hydro}, experienced by solid NH_3 particles, and maximum principal stress, σ_{max}, acting on the glass matrix were calculated using eqs (S20)−(S27) using the model illustrated in Figure S4 (see the SI). The simulation assumed a zero-strain state for the solid NH_3 particles within the glass matrix at 77 K and calculated the stress generated upon heating to 297 K. The result, indicated by the red diamond in Figure 2b, corresponds to a lattice parameter of 0.5150 nm, which is closer to the experimentally determined value of 0.5165 nm.[13] The estimated σ_{hydro} and σ_{max} are summarized in Table S5 (see the SI). Plotting σ_{hydro} (solid triangle) in Figure 4b indicates that the NH_3 particles experience compressive sub-GPa stress within the glass matrix consistent with the order of p_{trs} predicted from the thermodynamic estimation. Additional pressure likely results from interfacial tension between the solid NH_3 particles and boric glass matrix, as defined by the Young−Laplace equation.[68] Although the interfacial tension between solid NH_3(s) and the glass matrix is unknown, considering the nanoparticle size of NH_3(s) (37.8 nm), a certain additional hydrostatic stress can be expected.

Tschauner et al.[69] clarified that ice-VII is confined in natural diamond as inclusions and serves as an indicator for water-rich regions in Earth's deeper mantle. Ice-VII is a high-pressure form of water ice that is stable above 2.4 GPa.[69] This means robust matrices can confine substances which are stable under high pressures. The theoretical strength of a perfect crystal is defined as the force required to induce failure beyond interatomic interactions in an ideal crystal[70] and is estimated to be ∼ 9 GPa based on theoretical analysis of interatomic potentials. In contrast, the practical strengths of glasses are often reduced to one-hundredth or 1000th of their theoretical values due to the inherent formation of micro cracks that lead to failure.[71,72] The estimated σ_{max} value of 0.122 GPa appears to exceed the typical strengths of practical glasses.[71,72] However, localized nanosized regions in the glass matrix surrounding the NH_3 nanoparticles appear to exhibit a microcrack-free structure. As a result, the glass matrix likely endures the local σ_{max} caused by the difference in thermal expansion coefficient between itself and the NH_3 particles. Thus, one of the key reasons for the stabilization of NH_3(s) at ambient temperature is its confinement within an amorphous glass structure.

Beyond this pressure effect, the role of phase equilibria governing NH_3(s), the glass matrix (GM(gl)), and the impurity phase $NH_4B_5O_8{\cdot}4H_2O$(s) warrants further investigation. In the pseudo ternary NH_3(s)−GM(gl)−$NH_4B_5O_8{\cdot}4H_2O$(s) system, the solidus surface is generally known to shift to higher temperatures when a peritectic reaction occurs. To quantitatively evaluate this behavior, it is essential to determine not only the values of $\Delta_{mix}G^{\circ}_{m}$ for GM(gl) and $\Delta_{f}G^{\circ}_{m}$ for $NH_4B_5O_8{\cdot}4H_2O$(s) but also the Gibbs energy of substitution of boron into the nitrogen sites in NH_3(s). These unknown thermodynamic parameters must be systematically estimated in future studies to enable accurate phase equilibrium modeling and deepen our understanding of the NH_3(s) stabilization mechanism.

4. CONCLUSION

The current study elucidated the stabilization mechanism of solid-state ammonia, NH_3(s), confined within a boric acid glass matrix using a thermodynamic model supported by first-principles phonon calculation and hydrostatic stress analysis by micromechanics. Phonon calculations revealed vibrational DOS for the intermolecular translational and rotational modes of NH_3 molecules and intramolecular librational and bending modes of hydrogen atoms. The heat capacity of NH_3(s), $C^{\circ}_{p,m}$, was calculated from a Debye function accounting for the intermolecular translational and rotational modes of NH_3 and two Einstein functions accounting for the intramolecular librational and bending modes of hydrogen, regarding the DOS for these modes as the contribution ratios of the three functions. The standard Gibbs energy of formation of NH_3(s), $\Delta_{f}G^{\circ}_{m}$, at 298.15 K, determined by inserting the optimum $C^{\circ}_{p,m}$ function into the thermodynamic cycle, was −7.650 (kJ(mol of compd.)$^{-1}$). From this value, the standard Gibbs energy of transition from gas to solid via liquid, $\Delta_{trs}G^{\circ}_{m}$, was calculated to be 8.669 (kJ(mol of compd.)$^{-1}$). Consequently, the pressure required for this phase transition, p_{trs}, was estimated to be in the order of sub-GPa. Micromechanical analysis indicated that this hydrostatic stress originates from the difference between the thermal expansion coefficients of NH_3(s) and the glass matrix and stabilizes the ammonia crystals within the matrix. The present findings open a new avenue for stabilizing nonequilibrium phases at ambient temperature. A future challenge for the practical application of solid ammonia is the discovery of an outer matrix that can facilitate the evolution of H_2(g) from the decomposition of NH_3(s) confined within the glass matrix.

■ ASSOCIATED CONTENT

Data Availability Statement

All data generated or analyzed during this study are included in the published article and its Supporting Information.

Supporting Information

The Supporting Information is available free of charge at https://pubs.acs.org/doi/10.1021/acsomega.5c09165.

Detailed methods and results for thermodynamic calculation, phonon mode simulation, and micromechanical pressure analysis (PDF)

■ AUTHOR INFORMATION

Corresponding Author

Masao Morishita − *Research Center for Structural Materials, National Institute for Materials Science, Tsukuba, Ibaraki 305-0047, Japan;* orcid.org/0000-0002-6330-3901; Email: MORISHITA.Masao@nims.go.jp

https://doi.org/10.1021/acsomega.5c09165
ACS Omega 2025, 10, 57684−57691

Authors

Terumasa Tadano − *Research Center for Magnetic and Spintronic Materials, National Institute for Materials Science, Tsukuba, Ibaraki 305-0047, Japan;* orcid.org/0000-0002-8132-2161

Yusuke Matsuoka − *Research Center for Structural Materials, National Institute for Materials Science, Tsukuba, Ibaraki 305-0047, Japan*

Taichi Abe − *Research Center for Structural Materials, National Institute for Materials Science, Tsukuba, Ibaraki 305-0047, Japan*

Complete contact information is available at: https://pubs.acs.org/10.1021/acsomega.5c09165

Author Contributions

M.M.: Conceived the idea, constructed the thermodynamic model, and wrote the paper. T.T.: Simulated the phonon modes by first-principles calculation. Y.M.: Simulated hydrostatic stress by micromechanics analysis. T.A.: Reviewed and validated the work and provided helpful discussions.

Notes

M.M. is Professor Emeritus at the University of Hyogo.
The authors declare no competing financial interest.

■ ACKNOWLEDGMENTS

This work was supported in part by a Grant-in-Aid for Scientific Research (grant number 24K08127) from the Japan Society for the Promotion of Science (JSPS), the Ministry of Education, Culture, Sports, Science and Technology (MEXT) program "Data Creation and Utilization-Type Material Research and Development Project" (grant number JPMXP1122715503), and a Grant for Scientific Research (grant number 2024-J-031) from Izumi Science and Technology Foundation.

■ REFERENCES

(1) Akiba, E. The Method of High-Density Hydrogen Storage and Transportation, Hydrogen Storage Method. *J. Combust. Soc. Jpn.* **2011**, *53*, 16−21.

(2) Schüth, F.; Palkovitzs, R.; Schölgl, R.; Su, D. S. Ammonia as a Possible Element in an Energy Infrastructure: Catalysts for Ammonia Decomposition. *Energy Environ. Sci.* **2012**, *5*, 6278−6289.

(3) Marnellos, G.; Stoukides, M. Ammonia Synthesis at Atmospheric Pressure. *Science* **1998**, *282*, 98−100.

(4) Sekine, Y.; Manabe, R. Reaction Mechanism of Low-Temperature Catalysis by Surface Protonics in an Electric Field. *Faraday Discuss.* **2021**, *229*, 341−357.

(5) Murakami, K.; Tanaka, Y.; Sakai, R.; Toko, K.; Ito, K.; Ishikawa, A.; Higo, T.; Yabe, T.; Ogo, S.; Ikeda, M.; Tsuneki, H.; Nakai, H.; Sekine, Y. The Important Role of N_2H Formation Energy for Low-Temperature Ammonia Synthesis in an Electric Field. *Catal. Today* **2020**, *351*, 119−124.

(6) Haruyama, T.; Namise, T.; Shimomizu, N.; Uemura, S.; Takatsuji, Y.; Hino, M.; Yamasaki, R.; Kamachi, T.; Kohno, M. Non-catalyzed One-step Synthesis of Ammonia from Atmospheric Air and Water. *Green Chem.* **2016**, *18*, 4536−4541.

(7) Muzammil, I.; Kim, Y.-N.; Kang, H.; Dinh, D. K.; Choi, S.; Jung, C.; Song, Y.-H.; Kim, E.; Kim, J. M.; Lee, D. H. Plasma Catalyst-Integrated System for Ammonia Production from H_2O and N_2 at Atmospheric Pressure. *ACS Energy Lett.* **2021**, *6*, 3004−3010.

(8) Yin, S. F.; Xu, B. Q.; Zhou, X. P.; Au, C. T. A Mini-Review on Ammonia Decomposition Catalysts for On-Site Generation of Hydrogen for Fuel Cell Application. *Appl. Catal., A.* **2004**, *227*, 1−9.

(9) Li, X. K.; Ji, W. J.; Zhao, J.; Wang, S. J.; Au, C. T. Ammonia Decomposition over Ru and Ni Catalysts Supported on Fumed SiO_2, MCM-41, and SBA-15. *J. Catal.* **2005**, *236*, 181−189.

(10) Ogasawara, K.; Nakano, T.; Kishida, K.; Ye, T. N.; Lu, Y.; Abe, H.; Niwa, Y.; Sasae, M.; Kitano, M.; Hosono, H. Ammonia Decomposition over CaNH-Supported Ni Catalysts via an NH_2−Vacancy-Mediated Mars−van Krevelen Mechanism. *ACS Catal.* **2021**, *11*, 11005−11015.

(11) Young, J. R. Purity of Hydrogen Permeating Through Pd, Pd-25% Ag, and Ni. *Rev. Sci. Instrum.* **1963**, *34*, 891−892.

(12) The Engineering Tool Box. https://www.engineeringtoolbox.com/ammonia-d_1413.html.

(13) Morishita, M.; Miyoshi, H.; Kawasaki, H.; Yanagita, H. Stabilisation of Solid-state Cubic Ammonia Confined in Glass Substance at Ambient Temperature under Atmospheric Pressure. *RSC Adv.* **2024**, *14*, 16128−16137.

(14) Shore, S. G.; Böddeker, K. W. Large Scale Synthesis of $H_3B(NH_3)_2^+BH_4^-$ and H_3NBH_3. *Inorg. Chem.* **1964**, *3*, 914−915.

(15) Staubitz, A.; Robertson, A. P. M.; Manners, I. Ammonia-Borane and Related Compounds as Dihydrogen Sources. *Chem. Rev.* **2010**, *110*, 4079−4124.

(16) Choi, H. Y.; Park, S. J.; Seo, D.; Baek, J.-M.; Song, H. D.; Jung, S. J.; Lee, K. J.; Kim, Y. L. Low-temperature Synthesis of Ammonia Borane Using Diborane and Ammonia. *Int. J. Hydrogen Energy* **2015**, *40*, 11779−11784.

(17) Morishita, M.; Nozaki, A.; Yamamoto, H.; Fukumuro, N.; Mori, M.; Araki, K.; Sakamoto, F.; Nakamura, A.; Yanagita, H. Catalytic Activity of Co-Nanocrystal-doped Tungsten Carbide Arising From an Internal Magnetic Field. *RSC Adv.* **2021**, *11*, 14063−14070.

(18) Hubbard, W. B. Interior of the Giant Planet. *Science* **1981**, *214*, 145−149.

(19) Ninet, S.; Datchi, F. High Pressure−High Temperature Phase Diagram of Ammonia. *J. Chem. Phys.* **2008**, *128*, No. 154508.

(20) Glavin, D. P.; Dworkin, J. P.; Alexander, C. M. O.; et al. Abundant Ammonia and Nitrogen-rich Soluble Organic Matter in Samples from Asteroid (101955) Bennu. *Nat. Astron.* **2025**, *9*, 199−210.

(21) Olovsson, I.; Templeton, D. H. X-ray Study of Solid Ammonia. *Acta Crystallogr.* **1959**, *12*, 832−836.

(22) Mills, R. L.; Llebenberg, D. H.; Pruzan, Ph. Phase Diagram and Transition Properties of Condensed Ammonia to 10 kbar. *J. Phys. Chem. A* **1982**, *86*, 5219−5222.

(23) Von Dreele, R. B.; Hanson, R. C. Structure of NH_3-III at 1.28 GPa and Room Temperature. *Acta Crystallogr., Sect. C:Cryst. Struct. Commun.* **1984**, *40*, 1635−1638.

(24) Nye, C. L.; Medina, F. D. Temperature Dependence of the Raman Spectrum of Ammonia Solid I. *J. Chem. Phys.* **1987**, *87*, 6890−6894.

(25) Gauthier, M.; Pruzan, P.; Chervin, J. C.; Besson, J. M. Raman Scattering Study of Ammonia up to 75 GPa: Evidence for Bond Symmetrization at 60 GPa. *Phys. Rev. B* **1988**, *37*, No. 2102.

(26) Loveday, J. S.; Nelmes, R. J.; Marshal, W. G.; Besson, J. M.; Klotz, S.; Hamel, G. Structure of Deuterated Ammonia IV. *Phys. Rev. Lett.* **1996**, *76*, No. 74.

(27) Boese, R.; Niederprüm, N.; Bläser, D.; Maulitz, A.; Antipin, M. Y.; Mallinson, P. R. Single-Crystal Structure and Electron Density Distribution of Ammonia at 160 K on the Basis of X-ray Diffraction Data. *J. Phys. Chem. B* **1997**, *101* (30), 5794−5799.

(28) Enginer, Y.; Salihoglu, S.; Yurtensen, H. *T-P* Phase Diagram of Ammonia Solid Phases I, II and III. *Mater. Chem. Phys.* **2002**, *73*, 57−61.

(29) Fortes, A. D.; Brodholt, J. P.; Wood, I. G.; Vocadlo, L. Hydrogen Bonding in Solid Ammonia from ab Initio Calculations. *J. Chem. Phys.* **2003**, *118*, 5987−5994.

(30) Glasser, L. Equation of State and Phase Diagrams of Ammonia. *J. Chem. Educ.* **2009**, *86*, No. 1457.

(31) Ninet, S.; Datchi, F. Problem Disorder and Superionicity in Hot Dence Ammonia Ice. *Phys. Rev. Lett.* **2012**, *108*, No. 165702.

(32) Yu, X.; Jiang, X.; Su, Y.; Zhao, J. Compressive Behaviour and Electric Properties of Ammonia Ice: a First-principles Study. *RSC.Adv.* **2020**, *10*, 26579−26587.
(33) Cullity, B. D. *Elements of X-ray Diffraction*, 2nd ed.; Matsuula, G., Ed.; Addison-Wesley Publishing Company Inc., 1991; pp 322−337.
(34) Cox, J. P.; Wagman, D. D.; Medvedev, V. A. *CODATA Key Values for Thermodynamics*; Hemisphere Publ. Corp.: New York, 1989; Vol. *23*, pp 188−189.
(35) Overstreet, R.; Giauque, W. F. Ammonia. The Heat Capacity and Vapor Pressure of Solid and Liquid. Heat of Vaporization. The Entropy Values from Thermal and Spectroscopic Data. *J. Am. Chem. Soc.* **1937**, *59*, 254−259.
(36) Shi, Q.; Zhang, L.; Schlesinger, M. E.; Boerio-Goates, J.; Woodfileld, B. F. Low Temperature Heat Capacity Study of $FePO_4$ and Fe $_3(P_2O_7)_2$. *J. Chem. Thermodyn.* **2013**, *62*, 35−42.
(37) Morishita, M.; Kinoshita, Y.; Houshiyama, H.; Nozaki, A.; Yamamoto, H. Thermodynamic Properties for Calcium Molybdate, Molybdenum Tri-oxide and Aqueous Molybdate Ion. *J. Chem. Thermodyn.* **2017**, *114*, 30−43.
(38) Morishita, M.; Kinoshita, Y.; Tanaka, H.; Nozaki, A.; Yamamoto, H. Thermodynamic Properties for $Sm_2(MoO_4)_3$: Standard Entropy; Neel Temperature; Solubility Product. *Monatsh. Chem.* **2018**, *149*, 341−356.
(39) Morishita, M.; Kinoshita, Y.; Nozaki, A.; Yamamoto, H. Thermodynamic Properties for $MMoO_4$ (M = Mg, Sr and Ba) as the End-members of the Yellow Phases Formed in the Nuclear Fuel Waste Glasses. *Appl. Geo-Chem.* **2018**, *98*, 310−320.
(40) Kinoshita, Y.; Morishita, M.; Nozaki, A.; Yamamoto, H. Thermodynamic Properties for Neodymium Molybdate. *Mater. Trans.* **2019**, *60*, 111−120.
(41) Morishita, M.; Abe, T.; Nozaki, A.; Ohnuma, I.; Kamon, K. Calorimetric Study of $Nd_2Fe_{14}B$: Heat Capacity, Standard Gibbs Energy of Formation and Magnetic Entropy. *Thermochim. Acta* **2020**, *690*, No. 178672.
(42) Morishita, M.; Abe, T.; Yamamoto, H.; Nozaki, A.; Kimura, S. Thermodynamic and Magnetic Properties for $Dy_2Fe_{14}B$ Determined by Heat Capacity Measurement from Very Low to High Temperatures and Solution Calorimetry. *Thermochim. Acta* **2023**, *721*, No. 179410.
(43) Morishita, M.; Abe, T.; Ohkubo, T.; Tadano, T.; Yamamoto, H.; Nozaki, A.; Miyazaki, H. Magnetic Characterization of $Sm(Fe_{1-x}Cox)_{11}Ti$ (x = 0, 0.1) Determined by Heat-Capacity Measurement from Very Low to High Temperatures. *Thermochim. Acta* **2023**, *727*, No. 179573.
(44) Hoban, C.; Parkinson, N.; Jayanthi, K.; Paranthaman, M. P.; Navrotsky, A.; Woodfield, B. F. Impact of Anions and Water Content on [Li-Al] Layered Double-Hydroxide Stability. *J. Phys. Chem. C* **2025**, *129*, 793−800.
(45) Kittel, C. *Introduction to Solid State Physics*, 7th ed.; Wiley and Sons: Maruzen, Tokyo, 1998; pp 135−140.
(46) Bagatskii, M. I.; Kucheryavy, V. A.; Manzhelii, V. G.; Popop, V. A. Thermal Capacity of Solid Nitrogen. *Phys. Status Solidi B* **1968**, *26*, 453−460.
(47) Manzhelii, V. G.; Tolkachev, A. M.; Bagatskii, M. I.; Voitovich, E. I. Thermal Expansion, Heat Capacity, and Compressibility of Solid CO_2. *Phys. Stat. Solidi B* **1971**, *44*, 39−49.
(48) Popov, V. A.; Manzhelii, V. G.; Bagatskii, M. I. Heat Capacity of Solid NH_3. *J. Low Temp. Phys.* **1971**, *5*, 427−433.
(49) Berezin, B. Ya.; Ckekhovski, V. Ya.; Sheindlin, A. E. Enthalpy of Solid and Liquid Molybdenum by Levitation Calorimetry. *High Temp. - High Pressures* **1971**, *3*, 287−297.
(50) Tadano, T.; Gohda, Y.; Tsuneyuki, S. Anharmonic Force Constants Extracted from First-Principles Molecular Dynamics: Applications to Heat Transfer Simulations. *J. Phys.:Condens. Matter* **2014**, *26*, No. 225402.
(51) Kresse, G.; Furthmüller, J. Efficient Iterative Schemes for Ab Initio Total-Energy Calculations Using a Plane-Wave Basis Set. *Phys. Rev. B* **1996**, *54*, No. 11169.
(52) Kresse, G.; Joubert, D. From Ultrasoft Pseudopotentials to the Projector Augmented-Wave Method. *Phys. Rev. B* **1999**, *59*, No. 1758.
(53) Perdew, J. P.; Burke, K.; Ernzerhof, M. Generalized Gradient Approximation Made Simple. *Phys. Rev. Lett.* **1996**, *77*, No. 3865.
(54) Caldeweyher, E.; Ehlert, S.; Hansen, A.; Neugebauer, H.; Spicher, S.; Bannwarth, C.; Grimme, S. A Generally Applicable Atomic-Charge Dependent London Dispersion Correction. *J. Chem. Phys.* **2019**, *150* (15), No. 154122.
(55) Fisher, R. A.; Bouquet, F.; Phillips, N. E.; Franck, J. P.; Zhang, G.; Gordon, J. E.; Marcenat, C. Electron, Spin-wave, Hyperfine, and Phonon Contributions to the Low-temperature Specific Heat of $La_{0.65}Ca_{0.35}MnO_3$: Effects of Magnetic Fields and $^{16}O/^{18}O$ Exchange. *Phys. Rev. B* **2001**, *64*, No. 134425.
(56) Ott, J. B.; Boerio-Goates, J. *Chemical Thermodynamics: Principles and Applications*; Academic Press: San Diego, 2000; Vol. *218*, pp 285−287 0-12-530990-2.
(57) Wang, Y. U.; Jin, Y.; Khachaturyan, A. Phase Field Microelasticity Theory and Modeling of Elastically and Structurally Inhomogeneous Solid. *J. Appl. Phys.* **2002**, *92*, 1351−1360.
(58) Hu, S. Y.; Chen, L. Q. A Phase-field Model for Evolving Microstructures with Strong Elastic Inhomogeneity. *Acta Mater.* **2001**, *49*, 1879−1890.
(59) Ramos, M.; Moreno, J.; Vieira, S.; Prieto, C.; Fernández, J. Correlation of Elastic, Acoustic and Thermodynamic Properties in B_2O_3 Glasses. *J. Non-Cryst. Solids* **1997**, *221*, 170−180.
(60) Carini, G.; Carini, G.; D'angelo, G.; Tripodo, G.; Salvato, G.; Vasi, C.; Gilioli, E. Structural Transformations, Elastic Moduli and Thermal Expansion of Permanently Compacted B_2O_3 glasses. *J. Non-Cryst. Solids* **2014**, *401*, 40−43.
(61) Pinango, E. S.; Hortal, M.; Vieira, S.; Villar, R. The Low-temperature Thermal Expansion and Specific Heat of Glassy B_2O_3 and Two Glassy Sodium Borates. *J. Phys. C: Solid State Phys.* **1987**, *20*, 1−7.
(62) Qu, J.; Cherkaoui, M. *Fundamentals of Micromechanics of Solids*; Wiley: NJ, 2006; Vol. *79*.
(63) Perdew, J. P.; Ruzsinszky, A.; Csonka, G. I.; Vydrov, O. A.; Scuseria, G. E.; Constantin, L. A.; Zhou, X.; Burke, K. Restoring the Density-Gradient Expansion for Exchange in Solids and Surfaces. *Phys. Rev. Lett.* **2008**, *100* (13), No. 136406.
(64) Furness, J. W.; Kaplan, A. D.; Ning, J.; Perdew, J. P.; Sun, J. Accurate and Numerically Efficient r2SCAN Meta-Generalized Gradient Approximation. *J. Phys. Chem. Lett.* **2020**, *11*, 8208−8215.
(65) Ning, J.; Kothakonda, M.; Furness, J. W.; Kaplan, A. D.; Ehlert, S.; Brandenburg, J. G.; Perdew, J. P.; Sun, J. Workhorse Minimally Empirical Dispersion-Corrected Density Functional with Tests for Weakly Bound Systems: r2SCAN+rVV10. *Phys. Rev. B* **2022**, *106*, No. 075422.
(66) McHale, J. M.; Aurox, A.; Perrotta, J.; Navrotsky, A. Surface Energies and Thermodynamic Phase Stability in Nanocrystalline Aluminas. *Science* **1997**, *277*, 788−791.
(67) Navrotsky, A. Nanoscale Effects on Thermodynamics and Phase Equilibria in Oxide System. *ChemPhysChem* **2011**, *12*, 2207−2215.
(68) Gennes, P. de.; Brochard-Wyart, F.; Quéré, D. *Capillarity and Wetting Phenomena*; Springer: Heidelberg, 2004; Vol. *52*.
(69) Tschauner, O.; Huang, S.; Greenberg, E.; Prakapenska, V. R.; Ma, C.; Rossman, G. R.; Shen, A. H.; Zhang, D.; Newville, M.; Lanzirotti, A.; Tait, K. Ice-VII Incusions in Diamonds: Evidence for Aqueous Fluid in Earth's Deep Mantle. *Science* **2018**, *359*, 1136−1139.
(70) Milstein, F. Theoretical Strength of a Perfect Crystal. *Phys. Rev. B* **1971**, *3*, No. 1130.
(71) Griffits, A. A. VI. The Phenomena of Rupture and Flow in Solids. *Philos. Trans. R. Soc., A* **1921**, *221*, 163−198.
(72) Kiener, D.; Han, S. M. 100 Years After Griffith: From Brittle Bulk Fracture to Failure in 2D Materials. *MRS Bull.* **2022**, *47*, 792−799.

https://doi.org/10.1021/acsomega.5c09165
ACS Omega 2025, 10, 57684−57691

Mechanism of Solid Ammonia Stabilization at Ambient Temperature: Insights from Thermodynamics, Phonon Calculation, and Micromechanics

Masao Morishita [a]*, *Terumasa Tadano* [b], *Yusuke. Matsuoka* [a], *and Taichi Abe* [a]

[a] Research Center for Structural Materials, National Institute for Materials Science, 1-2-1 Sengen, Tsukuba, Ibaraki 305-0047, Japan

[b] Research Center for Magnetic and Spintronic Materials, National Institute for Materials Science, 1-2-1 Sengen, Tsukuba, Ibaraki 305-0047, Japan

*Email: MORISHITA.Masao@nims.go.jp

Supporting Information

METHODS

Assessment of thermodynamic data for solid-state ammonia

At the boiling point (239.7 K), the standard Gibbs energy of formation, $\Delta_{\mathrm{f}}G_{\mathrm{m}}^{\circ}$, of gaseous ammonia, $\mathrm{NH_3(g)}$, is represented by Equation (S1):

$$\Delta_{\mathrm{f}}G_{\mathrm{m}}^{\circ}(\mathrm{NH_3(g)},\ 239.7\ \mathrm{K}) = \Delta_{\mathrm{f}}G_{\mathrm{m}}^{\circ}(\mathrm{NH_3(g)},\ 298.15\ \mathrm{K}) + \int_{298.15}^{239.7} C_{p,\mathrm{m}}^{\circ}\left(\mathrm{NH_3(g)}\right)\mathrm{d}T$$

$$-\frac{1}{2}\int_{298.15}^{239.7} C_{p,\mathrm{m}}^{\circ}\left(\mathrm{N_2(g)}\right)\mathrm{d}T - \frac{3}{2}\int_{298.15}^{239.7} C_{p,\mathrm{m}}^{\circ}\left(\mathrm{H_2(g)}\right)\mathrm{d}T \qquad \text{(S1)}$$

$$-T\left\{\int_{298.15}^{239.7}\frac{C_{p,\mathrm{m}}^{\circ}\left(\mathrm{NH_3(g)}\right)}{T}\mathrm{d}T - \frac{1}{2}\int_{298.15}^{239.7}\frac{C_{p,\mathrm{m}}^{\circ}\left(\mathrm{N_2(g)}\right)}{T}\mathrm{d}T - \frac{3}{2}\int_{298.15}^{239.7}\frac{C_{p,\mathrm{m}}^{\circ}\left(\mathrm{H_2(g)}\right)}{T}\mathrm{d}T\right\}.$$

Liquid ammonia, $\mathrm{NH_3(l)}$, equilibrates with $\mathrm{NH_3(g)}$ at the boiling point. Therefore, the $\Delta_{\mathrm{f}}G_{\mathrm{m}}^{\circ}$ of the liquid phase is equal to that of the gas phase, as seen in Equation (S2):

$$\Delta_{\mathrm{f}}G_{\mathrm{m}}^{\circ}(\mathrm{NH_3(l)},\ 239.7\ \mathrm{K}) = \Delta_{\mathrm{f}}G_{\mathrm{m}}^{\circ}(\mathrm{NH_3(g)},\ 239.7\ \mathrm{K}). \qquad \text{(S2)}$$

At the melting point (195.4 K), the $\Delta_{\mathrm{f}}G_{\mathrm{m}}^{\circ}$ of the liquid phase is represented by Equation (S3):

$$\Delta_{\mathrm{f}}G_{\mathrm{m}}^{\circ}(\mathrm{NH_3(l)},\ 195.4\ \mathrm{K}) = \Delta_{\mathrm{f}}G_{\mathrm{m}}^{\circ}(\mathrm{NH_3(l)},\ 239.7\ \mathrm{K}) + \int_{239.7}^{195.4} C_{p,\mathrm{m}}^{\circ}\left(\mathrm{NH_3(l)}\right)\mathrm{d}T$$

$$-\frac{1}{2}\int_{239.7}^{195.4} C_{p,\mathrm{m}}^{\circ}\left(\mathrm{N_2(g)}\right)dT - \frac{3}{2}\int_{239.7}^{195.4} C_{p,\mathrm{m}}^{\circ}\left(\mathrm{H_2(g)}\right)dT$$

$$-T\left\{\int_{239.7}^{195.4}\frac{C_{p,\mathrm{m}}^{\circ}\left(\mathrm{NH_3(l)}\right)}{T}dT - \frac{1}{2}\int_{239.7}^{195.4}\frac{C_{p,\mathrm{m}}^{\circ}\left(\mathrm{N_2(g)}\right)}{T}dT - \frac{3}{2}\int_{239.7}^{195.4}\frac{C_{p,\mathrm{m}}^{\circ}\left(\mathrm{H_2(g)}\right)}{T}dT\right\}. \qquad \text{(S3)}$$

Solid-phase ammonia, $NH_3(s)$, equilibrates with $NH_3(l)$ at the boiling point. Therefore, the $\Delta_f G_m^\circ$ of the solid phase is equal to that of the liquid phase, as seen in Equation (S4),

$$\Delta_f G_m^\circ(NH_3(s),\ 195.4\ K) = \Delta_f G_m^\circ(NH_3(l),\ 195.4\ K). \quad (S4)$$

In Equations (S1)–(S4), values for $\Delta_f G_m^\circ(NH_3(g),\ 298.15\ K)$, $C_{p,m}^\circ(NH_3(g))$, $C_{p,m}^\circ(N_2(g))$, and $C_{p,m}^\circ(H_2(g))$ were adopted from CODATA,[34] while the value for $\Delta_f G_m^\circ(NH_3(l))$ was taken from the report by Overstreet and Giauque.[35]

Computational details of first-principles calculation

To compute the phonon band structure, density of states (DOS), and the temperature-dependent lattice constants of the type-I solid NH_3, we conducted first-principles calculations based on density functional theory (DFT) using the *Vienna Ab initio Simulation Package* (VASP)[51,52]. First, we optimized the lattice parameters and internal atomic coordinates until the residual forces on all atoms were below 0.001 eV/Å. We employed a kinetic energy cutoff of 520 eV, a convergence tolerance of 10^{-8} eV for self-consistent field iterations, and a $9 \times 9 \times 9$ Gamma-centered *k* points for the Brillouin zone sampling. Subsequently, we constructed a $3 \times 3 \times 3$ supercell containing 432 atoms from the optimized primitive cell. Each atom in this supercell was displaced from its equilibrium position by 0.01 Å, and the resulting atomic forces were calculated using VASP. The second-order interatomic force constants (IFCs) were determined by fitting the displacement-force dataset. Phonon frequencies $\{\omega_{\boldsymbol{q}\nu}\}$ within the harmonic approximation were obtained by diagonalizing the dynamical matrix constructed from these IFCs. To account for the long-range dipole-dipole interaction, we employed the Ewald summation technique using the dielectric tensor and the Born effective charges computed using density functional perturbation theory (DFPT). The IFC and phonon calculations were performed using the ALAMODE software[50].

To obtain the temperature-dependent lattice constants $a(T)$, bulk modulus $B(T)$, and the heat capacity at constant pressure $C_p(T)$, we performed phonon calculations at 11 different lattice constants: $a_0, 1.01a_0, 1.02a_0, \ldots, 1.10a_0$, where a_0 is the DFT-optimized lattice constant. From

the calculated electronic ground-state energy $U_0(a_i)$ and phonon frequencies $\{\omega_{\boldsymbol{q}\nu}(a_i)\}$, the Helmholtz free energy at lattice constant a_i (the corresponding volume V_i) was obtained as

$$F(V_i,T) = U_0(V_i) + F_{\mathrm{vib}}(V_i,T), \tag{S5}$$

where $F_{\mathrm{vib}}(V,T)$ is the vibrational free energy defined as

$$F_{\mathrm{vib}}(V,T) = \sum_{\boldsymbol{q}\nu}\left[\frac{\hbar\omega_{\boldsymbol{q}\nu}(V)}{2} + k_{\mathrm{B}}T\ln\left(1-e^{-\hbar\omega_{\boldsymbol{q}\nu}(V)/k_{\mathrm{B}}T}\right)\right]. \tag{S6}$$

A q point mesh of $30\times30\times30$ was employed in Eq. (S6). The equilibrium volume (V_{eq}), bulk modulus (B_{eq}), and its pressure derivative ($B_{eq}^{'}$) were determined by fitting the calculated free energies $F(V_i,T)$ to the Birch–Murnaghan equation of state:

$$E(\eta) = E_0 + \frac{9B_{\mathrm{eq}}V_{\mathrm{eq}}}{16}(\eta^2-1)^2\left[6+B'_{\mathrm{eq}}(\eta^2-1)-4\eta^2\right]. \tag{S7}$$

Here, $\eta = (V/V_0)^{1/3} = a/a_0$. By repeating the above procedure across various temperatures, we obtained the temperature-dependent lattice constants $a(T)$ and bulk modulus $B(T)$. The heat capacity $C_p(T)$ was evaluated as

$$C_p(T,p) = C_V(V(p,T),T) + T\frac{\partial V(p,T)}{\partial T}\frac{\partial S(V,T)}{\partial V}\Big|_{V=V(p,T)}, \tag{S8}$$

where C_V and $\partial S/\partial V$ at $V=V(p,T)$ were obtained by fitting polynomial functions to discrete values of $C_V(V_i)$ and vibrational entropy $S_{\mathrm{vib}}(V_i)$.

Assessment of pressure to stabilize solid-state ammonia at ambient temperature

At 298.15 K, the change in Gibbs energy of condensation under the pressure p_{con}, which drives the transition from gas to liquid, is expressed as Equation (S9):

$$\Delta G_p(\mathrm{g} \rightarrow \mathrm{l}) = \{\mu_{\mathrm{f}}(\mathrm{l}) - \mu^{\circ}(\mathrm{l})\} - \{\mu_{\mathrm{f}}(\mathrm{g}) - \mu^{\circ}(\mathrm{g})\} = -RT\ln\frac{p_{\mathrm{con}}}{p^{\circ}}, \quad \text{(S9)}$$

where the first term, $\{\mu_{\mathrm{f}}(\mathrm{l}) - \mu^{\circ}(\mathrm{l})\}$, is the change in the chemical potential of liquid-phase due to pressurization. Generally, the change in the chemical potential of a condensed phase under pressing during condensation is negligibly small.[56] Therefore, this first term was neglected. The second term, $\{\mu_{\mathrm{f}}(\mathrm{g}) - \mu^{\circ}(\mathrm{g})\}$, denotes the change in the chemical potential of the gas phase with pressurization and is expressed as $RT\ln\frac{p_{\mathrm{f}}}{p^{\circ}}$. On the other hand, at 298.15 K, the standard Gibbs energy of condensation, $\Delta_{\mathrm{con}}G^{\circ}_{\mathrm{m}}$, from liquid to solid is defined by Equation (S10):

$$\Delta_{\mathrm{con}}G^{\circ}_{\mathrm{m}} = \Delta_{\mathrm{f}}G^{\circ}_{\mathrm{m}}(\mathrm{NH_3(l)},\ 298.15\ \mathrm{K}) - \Delta_{\mathrm{f}}G^{\circ}_{\mathrm{m}}(\mathrm{NH_3(g)},\ 298.15\ \mathrm{K}). \quad \text{(S10)}$$

The first term, $\Delta_{\mathrm{f}}G^{\circ}_{\mathrm{m}}(\mathrm{NH_3(l)},\ 298.15\ \mathrm{K})$, is defined by Equation (S11):

$$\Delta_{\mathrm{f}}G^{\circ}_{\mathrm{m}}(\mathrm{NH_3(l)},\ 298.15\ \mathrm{K}) = \Delta_{\mathrm{f}}G^{\circ}_{\mathrm{m}}(\mathrm{NH_3(l)},\ 195.4\ \mathrm{K}) + \int_{195.4}^{298.15} C^{\circ}_{p,\mathrm{m}}\big(\mathrm{NH_3(l)}\big)\mathrm{d}T$$

$$-\frac{1}{2}\int_{195.4}^{298.15} C^{\circ}_{p,\mathrm{m}}\big(\mathrm{N_2(g)}\big)\mathrm{d}T - \frac{3}{2}\int_{195.4}^{298.15} C^{\circ}_{p,\mathrm{m}}\big(\mathrm{H_2(g)}\big)\mathrm{d}T \quad \text{(S11)}$$

$$-T\left\{\int_{195.4}^{298.15}\frac{C^{\circ}_{p,\mathrm{m}}\big(\mathrm{NH_3(l)}\big)}{T}\mathrm{d}T - \frac{1}{2}\int_{195.4}^{298.15}\frac{C^{\circ}_{p,\mathrm{m}}\big(\mathrm{N_2(g)}\big)}{T}\mathrm{d}T - \frac{3}{2}\int_{195.4}^{298.15}\frac{C^{\circ}_{p,\mathrm{m}}\big(\mathrm{H_2(g)}\big)}{T}\mathrm{d}T\right\}.$$

Here, the first term of right side, $\Delta_{\mathrm{f}}G_{\mathrm{m}}^{\circ}(\mathrm{NH_3(l)},\ 195.4\ \mathrm{K})$, is given by Equation (S11) described above. The extrapolated function fitting $C_{p,\mathrm{m}}^{\circ}\left(\mathrm{NH_3(l)}\right)$[35] was optimized and expressed in the footnote of Table S2 below.

Thus, $\Delta_{\mathrm{f}}G_{\mathrm{m}}^{\circ}(\mathrm{NH_3(l)},\ 298.15\ \mathrm{K})$ was determined by inserting $\Delta_{\mathrm{f}}G_{\mathrm{m}}^{\circ}(\mathrm{NH_3(l)},\ 195.4\ \mathrm{K})$ and the optimized fitting function of $C_{p,\mathrm{m}}^{\circ}\left(\mathrm{NH_3(l)}\right)$ into Equation (S11). Hence, $\Delta_{\mathrm{con}}G_{\mathrm{m}}^{\circ}$ was determined.

Equating $\Delta_{\mathrm{con}}G_{\mathrm{m}}^{\circ}$ with $\Delta G_p(\mathrm{g}\rightarrow\mathrm{l})$ is expressed in Equation (S12):

$$\Delta_{\mathrm{con}}G_{\mathrm{m}}^{\circ}+\Delta G_p(\mathrm{g}\rightarrow\mathrm{l})=\ 0. \tag{S12}$$

Consequently, $\Delta_{\mathrm{con}}G_{\mathrm{m}}^{\circ}$ can be written as Equation (S13):

$$\Delta_{\mathrm{con}}G_{\mathrm{m}}^{\circ}=\{\mu_{\mathrm{f}}(\mathrm{g})-\mu^{\circ}(\mathrm{g})\}=RT\ln\frac{p_{\mathrm{con}}}{p^{\circ}}. \tag{S13}$$

From here, Equation (C5) is rewritten as Equation (S14):

$$\frac{p_{\mathrm{con}}}{p^{\circ}}=\exp\left(\frac{\Delta_{\mathrm{con}}G_{\mathrm{m}}^{\circ}}{RT}\right). \tag{S14}$$

Then, at 298.15 K, the change in Gibbs energy of freezing under the pressure p_{freez}, driving the transition from liquid to solid, is expressed as Equation (S15):

$$\begin{aligned}\Delta G_p(\mathrm{l}\rightarrow\mathrm{s})=&\ \{\mu_{\mathrm{f}}(\mathrm{s})-\mu^{\circ}(\mathrm{s})\}-\{\mu_{\mathrm{f}}(\mathrm{l})-\mu^{\circ}(\mathrm{l})\}\\ =&\ V_{\mathrm{m}}(\mathrm{s})\int_{p^{\circ}}^{p_{\mathrm{freez}}}dp-V_{\mathrm{m}}(\mathrm{l})\int_{p^{\circ}}^{p_{\mathrm{freez}}}dp\\ =&\ \{V_{\mathrm{m}}(\mathrm{s})-V_{\mathrm{m}}(\mathrm{l})\}\times\int_{p^{\circ}}^{p_{\mathrm{freez}}}dp\\ =&\ \{V_{\mathrm{m}}(\mathrm{s})-V_{\mathrm{m}}(\mathrm{l})\}\times(p_{\mathrm{freez}}-p^{\circ})\end{aligned} \tag{S15}$$

where $V_{\mathrm{m}}(\mathrm{s})$ and $V_{\mathrm{m}}(\mathrm{l})$ are the molar volumes of the solid and liquid phases, respectively. $V_{\mathrm{m}}(\mathrm{s})$ was taken as 2.07444×10^{-5} m^3 based on the described NH_3(s) confined in the glass matrix (GM) with a lattice constant of 0.5165 nm in our previous study.[13] $V_{\mathrm{m}}(\mathrm{l})$ was taken as 2.44690×10^{-5} m^3 from the reference data.[13] Therefore, the volume reduced by 3.72457×10^{6} m^3 through freezing. Although the $V_{\mathrm{m}}(\mathrm{s})$ and $V_{\mathrm{m}}(\mathrm{l})$ values were measured at 297.15 and 293.15 K, respectively, they were approximated as values at 298.15 K for our thermodynamic analyses.

The standard Gibbs energy of freezing, $\Delta_{\mathrm{freez}}G^{\circ}_{\mathrm{m}}$, is represented by Equation (S16):

$$\Delta_{\mathrm{freez}}G^{\circ}_{\mathrm{m}} = \Delta_{\mathrm{f}}G^{\circ}_{\mathrm{m}}(\mathrm{NH_3(s)},\ 298.15\ \mathrm{K}) - \Delta_{\mathrm{f}}G^{\circ}_{\mathrm{m}}(\mathrm{NH_3(l)},\ 298.15\ \mathrm{K}). \quad \text{(S16)}$$

Equating $\Delta_{\mathrm{freez}}G^{\circ}_{\mathrm{m}}$ with $\Delta G_p(\mathrm{l} \rightarrow \mathrm{s})$ provides Equation (S17):

$$\Delta_{\mathrm{freez}}G^{\circ}_{\mathrm{m}} + \Delta G_p(\mathrm{l} \rightarrow \mathrm{s}) = 0. \quad \text{(S17)}$$

Consequently, from Equations (S15)–(S17), the pressure, p_{freez}, driving the liquid to solid transition is given by Equation (S18):

$$p_{\mathrm{freez}} = \frac{\Delta_{\mathrm{freez}}G^{\circ}_{\mathrm{m}}}{\{V_{\mathrm{m}}(\mathrm{cr}) - V_{\mathrm{m}}(\mathrm{l})\}} + p^{\circ}. \quad \text{(S18)}$$

Hence, the pressure, p_{trs}, required to form solid from gas via the liquid phase is given by Equation (S19):

$$p_{\mathrm{sol}} = p_{\mathrm{con}} + p_{\mathrm{freez}}. \quad \text{(S19)}$$

Detail of micromechanical calculation

The stress field is described by the Hooke's law:

$$\sigma_{ij}(r) = C_{ijkl}(r)\varepsilon^{e}_{kl}(r) \quad \text{(S20)}$$

where σ_{ij} represents the stress tensor, C_{ijkl} is the local elastic modulus tensor, and ε^{e}_{kl} is the local elastic strain tensor.

The elastic modulus is expressed as

$$C_{ijkl}(r) = C^{0}_{ijkl} + \Delta C_{ijkl}\phi(r) \quad \text{(S21)}$$

Here, C^{0}_{ijkl} represents the elastic modulus of the B_2O_3 ($C^{B_2O_3}_{ijkl}$), and ΔC_{ijkl} denotes the difference in elastic moduli between B_2O_3 and NH_3 ($\Delta C_{ijkl} = C^{B_2O_3}_{ijkl} - C^{NH_3}_{ijkl}$). The function ϕ is a spatial indicator, with $\phi = 1$ inside the spherical particles and $\phi = 0$ outside. The elastic strain ε^{e}_{ij} is defined as

$$\varepsilon^{e}_{ij}(r) = \bar{\varepsilon}_{ij} + e^{c}_{ij}(r) - \varepsilon^{0}_{ij}(r) \quad \text{(S22)}$$

where $\bar{\varepsilon}_{ij}$ represents a uniform strain representing the average strain across the simulation domain, e^{c}_{ij} is the deviation from the average, computed using an iterative perturbation method,[58] and ε^{0}_{ij} is the eigenstrain. The thermal expansion of NH_3 is incorporated through the eigenstrain term:

$$\varepsilon^{0}_{ij}(r) = \eta\delta_{ij}\phi(r) \quad \text{(S23)}$$

where η represents the volumetric expansion of NH_3 due to temperature increase from 77 K to 297 K, and δ_{ij} is the Kronecker delta. η is calculated as

$$\eta = \frac{a_{297\mathrm{K}} - a_{77\mathrm{K}}}{a_{77\mathrm{K}}} \tag{S24}$$

The pressure within the particles was determined from the calculated stress field σ_{ij} as the hydrostatic stress, σ_{hydro}, at the particle center:

$$\sigma_{\mathrm{hydro}} = \frac{\sigma_{11} + \sigma_{22} + \sigma_{33}}{3} \tag{S25}$$

The change in the NH_3 lattice constant due to elastic strain was calculated using the elastic strain at the particle center $\varepsilon_{ij}^{\mathrm{e}}$:

$$a_{297\mathrm{K}}^{\mathrm{strained}} = a_{77\mathrm{K}}(1 + \varepsilon_{11}^{\mathrm{e}} + \varepsilon^{0}) \tag{S26}$$

Note that in the current configuration of isotropic elastic constant tensor and isotropic shape of particle, elastic strain also becomes isotropic and satisfies $\varepsilon_{11}^{\mathrm{e}} = \varepsilon_{22}^{\mathrm{e}} = \varepsilon_{33}^{\mathrm{e}}$. Therefore, $a_{297\mathrm{K}}^{\mathrm{strained}}$ can be calculated using any of $\varepsilon_{11}^{\mathrm{e}}$, $\varepsilon_{22}^{\mathrm{e}}$, $\varepsilon_{33}^{\mathrm{e}}$.

The maximum principal stress, denoted as σ_1, often serves as a fracture criterion for brittle materials such as glass. It is determined by solving the eigenvalue problem of the stress tensor σ_{ij}. The eigenvalues of σ_{ij}, corresponding to the principal stresses, are obtained by solving the characteristic equation:

$$\det(\sigma_{ij} - \sigma\delta_{ij}) = 0 \tag{S27}$$

The three real roots of this equation, ordered as $\sigma_1 \geq \sigma_2 \geq \sigma_3$, represent the principal stresses. The largest eigenvalue, σ_1, corresponds to the direction of maximum tensile stress within the material. To assess the risk of glass matrix fracture caused by thermal stress, we calculated the

maximum value, σ_{max}, of the computed σ_1 across the simulation domain and compared it with the mechanical strength of the glass material.

The calculations employed lattice constants a_{297K} and a_{77K} for NH_3 obtained from PBE+D4 calculations. The elastic properties of NH_3 were modeled assuming isotropic elasticity, employing a Poisson's ratio (ν) of 0.2 and volume modulus calculated by PBE+D4. To incorporate the pressure dependence of K, we fitted the calculated K data for different pressure to a second-order polynomial equation of the form $K(\varepsilon_v) = \kappa_\alpha \varepsilon_v^2 + \kappa_\beta \varepsilon_v + \kappa_\gamma$ where ε_v is the volumetric strain $\varepsilon_v (= (1 + \varepsilon_{11})(1 + \varepsilon_{22})(1 + \varepsilon_{33}) - 1)$. The stress and strain arising from the pure expansion of the spherical particle is uniform within the particle.[62] Therefore, the volumetric strain ε_v can be selected at any point within the particle. In the simulation, volumetric strain at the center of the spherical particle was selected as ε_v. For the elastic modulus of B_2O_3, the value measured by Ramos et al. [59] were employed. Table S1 summarizes the parameters used for the phase-field micromechanical elasticity simulation.

Table S1 Parameters used for the phase-field micromechanical elasticity simulation: Lattice constants, a_T, and coefficients for volume modulus of NH_3, κ_l, were determined from the present first principles calculation; elastic constants of B_2O_3, C_{ij}, were values given by Ramos et al.[59] Poisson ratio of NH_3, ν, from κ_l.

Parameter	Values	Remarks
$a_T(NH_3)$/nm	a_{297K} = 0.5279; a_{77K} = 0.5100	Present first principles cal.
$C_{ij}(B_2O_3)$/GPa	C_{11} = 24.42; C_{44} = 7.53	Ref. 59
$\kappa_l(NH_3)$/GPa	κ_α = 92.73; κ_β = 13.39; κ_γ = 2.34	Present first principles cal.
$\nu(NH_3)$	0.2	-

RESULTS

Coefficients for the $C^{\circ}_{p,\mathrm{m}}(\mathrm{NH_3(s)})$ fitting functions

Overstreet and Giauque[35] measured the $C^{\circ}_{p,\mathrm{m}}$ data for solid state ammonia at 15–190 K. Their data were fitted using the Debye–Einstein function given by Equation (2) in the main document. The coefficients for the optimized Debye–Einstein function are listed in Table S2.

Table S2. Coefficients for the optimized Debye–Einstein function fitted with $C^{\circ}_{p,\mathrm{m}}$ data over 15–190 K measured by Overstreet and Giauque.[35]

	Parameters	Coefficients
Low T fits	γ / (J K^{-2} mol of compd.$^{-1}$)	1.78959E–02
	B_3 / (J K^{-4} mol of compd.$^{-1}$)	8.86855E–05
	B_5 / (J K^{-6} mol of compd.$^{-1}$)	2.88074E–07
	B_7 / (J K^{-8} mol of compd.$^{-1}$)	–4.29667E–10
	B_9 / (J K^{-10} mol of compd.$^{-1}$)	2.35470E–13
	B_{11}/ (J K^{-12} mol of compd^{-1})	–4.63626E–17
	Range / K	0–33.18

Continued in the next page.

Continued from the previous page.

	Parameters	Coefficients
Mid *T* fits	C_0 / (J K^{-1} mol of compd.$^{-1}$)	–2.40083E+02
	C_1 / (J K^{-2} mol of compd.$^{-1}$)	2.89626E+01
	C_2 / (J K^{-3} mol of compd.$^{-1}$)	–1.43600E+00
	C_3 / (J K^{-4} mol of compd.$^{-1}$)	3.78861E–02
	C_4 / (J K^{-5} mol of compd.$^{-1}$)	–5.54968E–04
	C_5 / (J K^{-6} mol of compd^{-1})	4.28484E–06
	C_6 / (J K^{-7} mol of compd.$^{-1}$)	–1.36411E–08
	Range / K	33.18–71.58
High *T* fits	l	3.32700E–01
	θ_D / K	3.03501E+02
	m	3.33780E–01
	θ_{E_1} / K	5.29767E+03
	n	3.33490E–01
	θ_{E_2} / K	2.34982E+04
	A_1 / (J K^{-2} mol of compd.$^{-1}$)	2.44022E–02
	A_2 / (J K^{-4} mol of compd.$^{-1}$)	2.24768E–06
	Range/*T*	71.58–300

Deviations between experimental and calculated $C^{\circ}_{p,\mathrm{m}}(\mathrm{NH_3(s)})$

The deviations, $u_{\mathrm{fit}}(C^{\circ}_{p,\mathrm{m}})$, between the data calculated from the Debye–Einstein function (Equation (1) and Table S2) and the $C^{\circ}_{p,\mathrm{m}}$ data[35] were 1.34, 1.17, 1.45, and 1.30% at 15.0, 88.70, 93.4, and 103.0 K, respectively. At other temperatures, the $u_{\mathrm{fit}}(C^{\circ}_{p,\mathrm{m}})$ values were within one %.

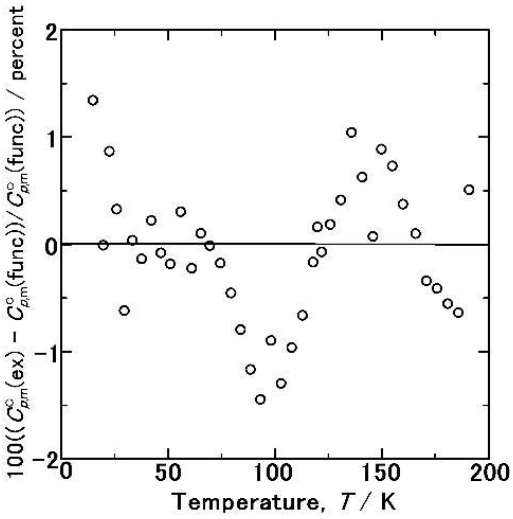

Figure S1. Deviations between experimental $C^{\circ}_{p,\mathrm{m}}$ data for solid ammonia (open circles) at 15–190 K and the results calculated from the fitting functions optimized in the present study (Equations (1)–(3) and Table S2).

Lattice constants and heat capacities from first-principles calculations

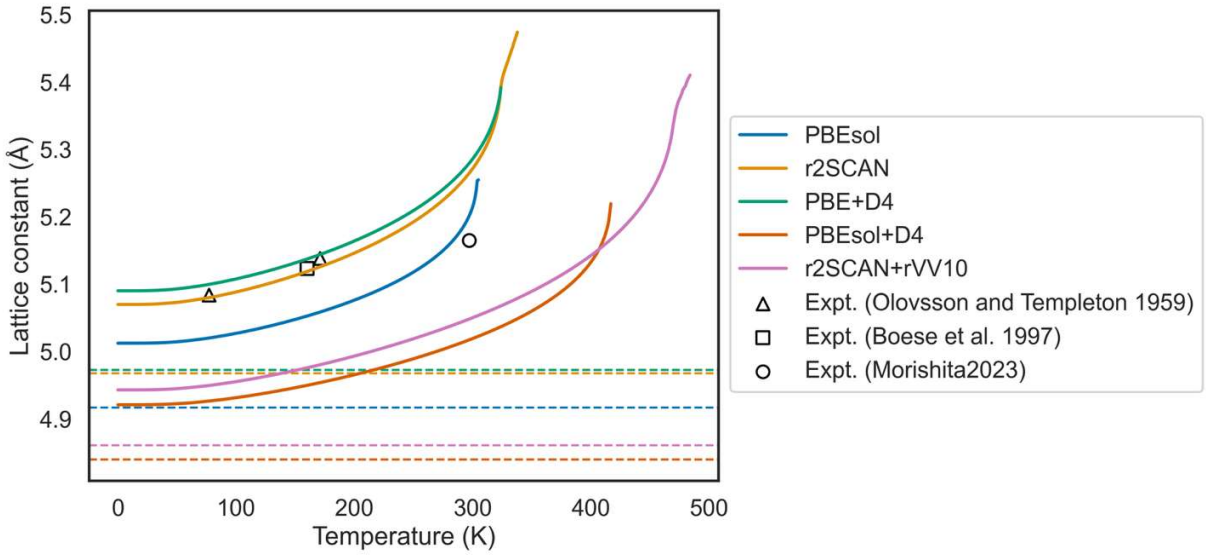

Figure S2. Temperature-dependent lattice constants computed using various exchange-correlation (XC) functionals compared with the experimental data. The solid lines represent the calculated results within the quasiharmonic approximation, whereas the dashed lines indicate the DFT-optimized lattice parameters. The tested XC functionals are PBEsol,[63] r2SCAN,[64] PBE+D4,[54] PBEsol+D4,[54] and r2SCAN+rVV10.[65]

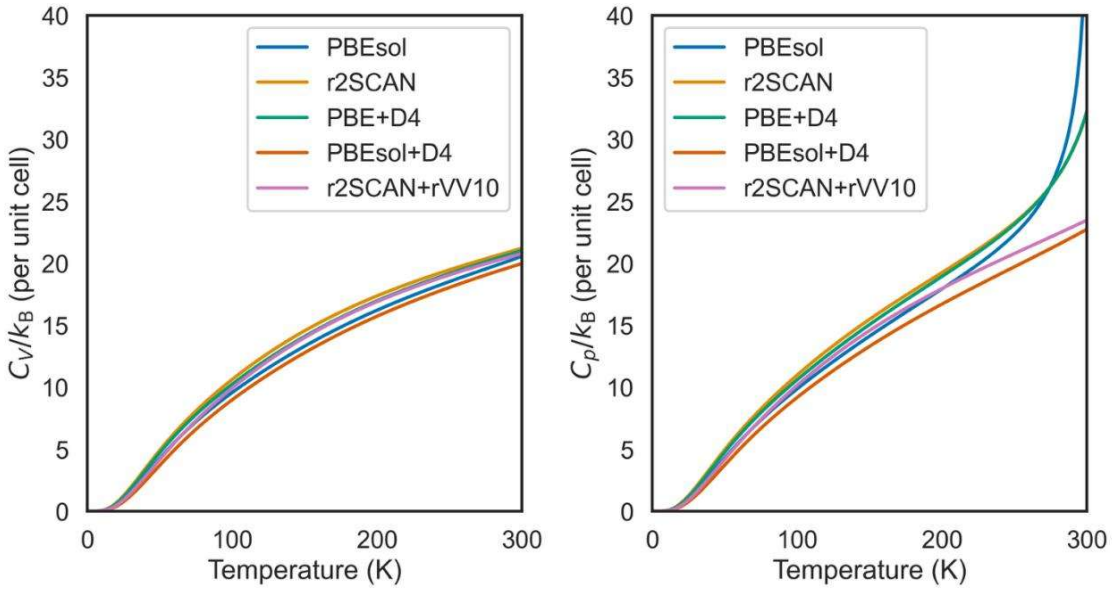

Figure S3. Heat capacity at the constant volume (left) and constant pressure (right) computed using first-principles lattice dynamics within the quasiharmonic approximation.

Thermodynamic data for solid, liquid, and gas phases

The thermodynamic functions for the solid, liquid, and gas phases at equilibrium are summarized in Table S3. The thermodynamic functions for the solid phase, including quasi-equilibrium states above 195.4 K, are summarized in Table S4.

The $\Delta_f G_m^\circ$ value of solid-phase ammonia at 298.15 K was determined by inserting the optimized Debye–Einstein function into Equation (1) in the main text.

Table S3. Thermodynamic values for solid, liquid, and gas phases of ammonia.

T / K	$C^{\circ}_{p,\mathrm{m}}$ / (J K^{-1} (mol compd.)$^{-1}$)	S°_{m} / (J K^{-1} (mol compd.)$^{-1}$)	$H^{\circ}_{\mathrm{m}}(T) - H^{\circ}_{\mathrm{m}}(298.15)$ / (kJ (mol compd.)$^{-1}$)	$\varphi(T)$ / (J K^{-1} (mol compd.)$^{-1}$)	$\Delta_{\mathrm{f}}H^{\circ}_{\mathrm{m}}$ / (kJ (mol compd.)$^{-1}$)	$\Delta_{\mathrm{f}}G^{\circ}_{\mathrm{m}}$ / (kJ (mol compd.)$^{-1}$)
Solid						
0	0	0	–39.157	Infinite	-	-
20	1.550	0.711	–39.148	0.713	-	-
50	11.130	5.626	–38.965	5.627	-	-
100	26.495	18.288	–38.007	18.288	–72.860	–51.611
150	38.527	31.329	–36.379	31.329	–73.980	–41.204
195.4	51.049	43.027	–34.358	43.027	–74.460	–30.661
Liquid*1						
195.4	73.339	71.968	–28.703	71.968	–68.804	–30.661
200	73.614	73.678	–28.365	73.678	–68.714	–29.671
239.7	75.981	87.215	–25.395	87.215	–68.006	–22.263
Gas*2						
239.7	34.515	184.632	–2.044	184.632	–44.655	–22.263
250	34.338	186.079	–1.690	186.079	–44.888	–21.301
298.15	34.547	192.258	0	192.258	–45.940	–16.319
300	35.678	192.479	0.066	192.479	–45.980	–16.136

*1 $\Delta_{\mathrm{f}}G^{\circ}_{\mathrm{m}}(\mathrm{l})/(\mathrm{kJ\ (mol\ of\ compd.)^{-1}}) = -68.139 + 0.1918T$

*2 $\Delta_{\mathrm{f}}G^{\circ}_{\mathrm{m}}(\mathrm{l})/(\mathrm{kJ\ (mol\ of\ compd.)^{-1}}) = -46.819 + 0.1023T$

Table S4. Thermodynamic values for solid phase ammonia.

T / K	$C_{p,\mathrm{m}}^{\circ}$ / (J K^{-1} (mol compd.)$^{-1}$)	S_{m}° / (J K^{-1} (mol compd.)$^{-1}$)	$H_{\mathrm{m}}^{\circ}(T)-H_{\mathrm{m}}^{\circ}(298.15)$ / (kJ (mol compd.)$^{-1}$)	$\varphi(T)$ / (J K^{-1} (mol compd.)$^{-1}$)	$\Delta_{\mathrm{f}}H_{\mathrm{m}}^{\circ}$ / (kJ (mol compd.)$^{-1}$)	$\Delta_{\mathrm{f}}G_{\mathrm{m}}^{\circ}$ / (kJ (mol compd.)$^{-1}$)
0	0	0	–12.195	Infinite	-	-
20	1.550	0.711	–12.186	0.712	-	-
50	11.130	5.626	–12.003	5.626	-	-
100	26.495	18.288	–11.046	18.288	–72.860	–51.611
150	38.527	31.329	–9.417	31.329	–73.980	–41.204
195.4	51.049	43.027	–7.396	43.027	–74.460	–30.661
200	52.528	44.232	–7.158	44.232	–74.469	–29.537
239.7	67.484	54.993	–4.79	54.993	–74.362	–20.895
250	72.092	57.928	–4.071	57.928	–74.230	–18.606
298.15	98.384	72.753	0	72.753	–72.902	–7.650
300	99.564	73.365	0.183	73.365	–72.825	–7.246

Hydrostatic stress for phase transitions at 298.15 K

Figs. S4(a), (b) and (c) shows the NH_3 article placed in the B_2O_3 matrix and calculated hydrostatic and maximum principal stress field, respectively. The NH_3 particles exhibited a uniform σ_{hydro} of 0.292 GPa. The maximum principal stress was compressive within the NH_3 particle, while the B_2O_3 matrix experienced tensile stresses, reaching a maximum value of 0.122

GPa at the particle/matrix interface. These results demonstrate that the NH_3 particles are subjected to sub-GPa thermal stresses, while B_2O_3 matrix experiences substantial tensile forces.

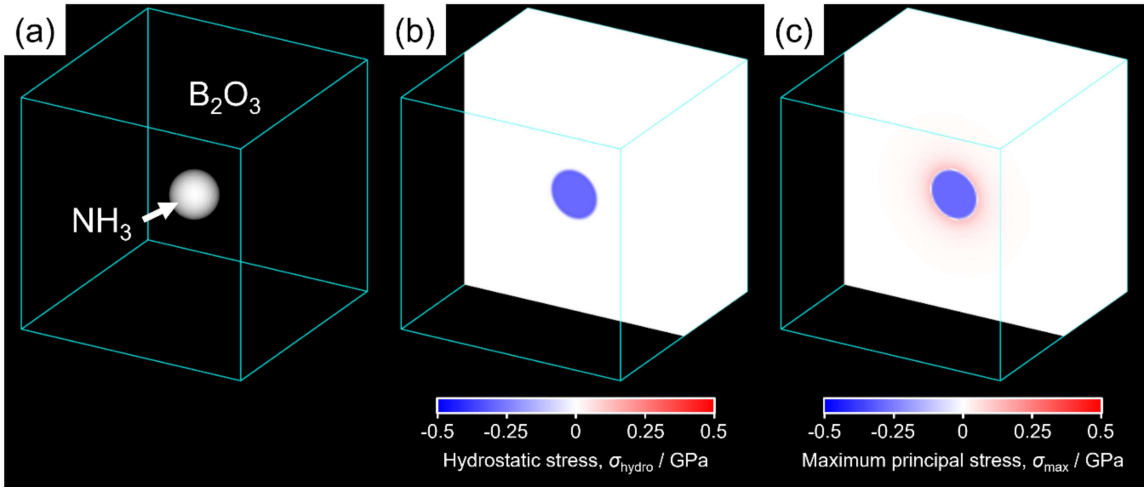

Figure S4. NH_3 article placed in the B_2O_3 matrix (a), and hydrostatic stress field (b) and maximum principal stress field (c) calculated by phase-field micromechanical elasticity simulation. Positive value (red) indicates tensile stress and negative value (blue) indicates compressive stress.

Table S5. Estimated hydrostatic stress, σ_{hydro}, experienced by the NH_3 particles and maximum principal stress, σ_{max}, acting on glass matrix (GM).

297 K	GPa	Remarks
$\sigma_{hydro}(NH_3(s))$	0.292	Compressive stress
$\sigma_{max}(GM)$	0.122	Tensile stress